Interfacial Electrochemistry of Catalyst-Coordinated Graphene Nanoribbons

Erik J. Askins[1,2], Pouyan Navabi[1], Khagesh Kumar[1], Sarah Jasmin Finkelmeyer[3,4], Martin Presselt[3,5,6], Jordi Cabana[1,7] and Ksenija D. Glusac[1,2*]

[1]*Department of Chemistry, University of Illinois Chicago, Chicago, Illinois 60607*

[2]*Chemical Sciences and Engineering Division, Argonne National Laboratory, Lemont, Illinois 60439*

[3]*Leibniz Institute of Photonic Technology (IPHT), Jena, Germany 07745*

[4]*Institute of Physical Chemistry, Friedrich Schiller University Jena, Jena, Germany 07743*

[5]*SciClus GmbH & Co. KG, Jena, Germany 07745*

[6]*Center for Energy and Environmental Chemistry Jena (CEEC Jena), Friedrich Schiller University, Jena, Germany 07743*

[7]*Materials Science Division, Argonne National Laboratory, Lemont, Illinois 60439*

*Corresponding author

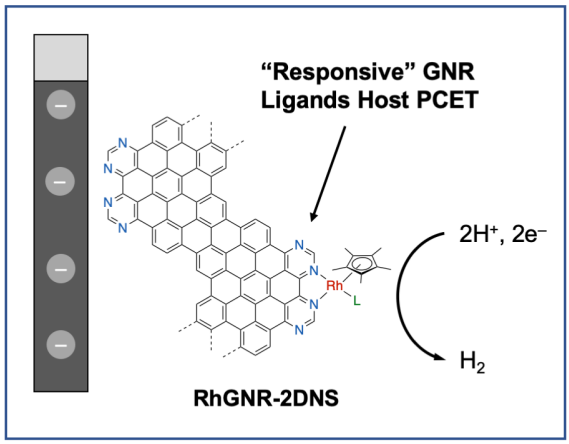

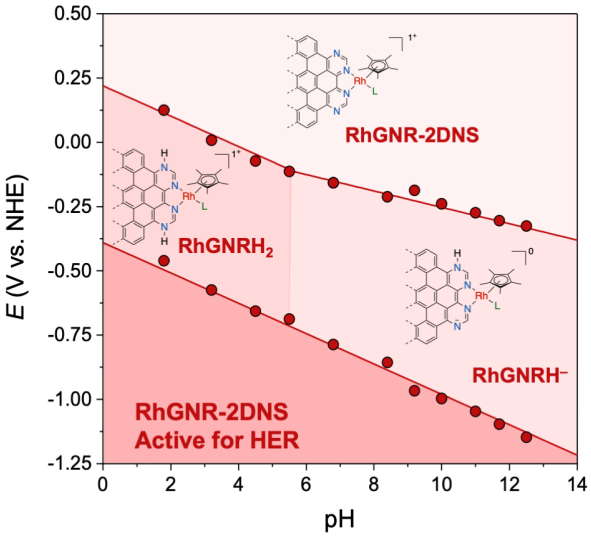

Abstract

The immobilization of molecular electrocatalysts on conductive electrodes is an appealing strategy for enhancing their overall activity relative to analogous molecular compounds. In this study we report on the interfacial electrochemistry of self-assembled 2D nanosheets of graphene nanoribbons (**GNR-2DNS**) and analogs containing a Rh-based hydrogen evolution reaction (HER) catalyst (**RhGNR-2DNS**) immobilized on conductive electrodes. Proton-coupled electron transfer (PCET) taking place at N-centers of the nanoribbons was utilized as an indirect reporter of the interfacial electric fields experienced by the monolayer nanosheet located within the electric

double layer. The experimental Pourbaix diagrams were compared with a theoretical model which derives the experimental Pourbaix slopes as a function of parameter ***f***, a fraction of the interfacial potential drop experienced by the redox-active group. Interestingly, our study revealed that **GNR-2DNS** was strongly coupled to glassy carbon electrodes (***f*** = 1), while **RhGNR-2DNS** was not (***f*** = 0.15). We further investigated the HER mechanism by **RhGNR-2DNS** using electrochemical and X-ray absorption spectroelectrochemical methods and compared it to the homogeneous molecular model compounds. **RhGNR-2DNS** was found to be an active HER electrocatalyst over a broader set of aqueous pH conditions than its molecular analogs. We find that the improved HER performance in the immobilized catalyst arises due to two factors. First, redox-active bipyrimidine-based ligands were shown to dramatically alter the activity of Rh sites by increasing the electron density at the active Rh center and providing **RhGNR-2DNS** the improved catalysis. Second, the catalyst immobilization was found to prevent catalyst aggregation that was found to occur for the molecular analog in the basic pH. Overall, this study provides valuable insights into the mechanistic by which catalyst immobilization can affect the overall electrocatalytic performance.

Introduction

Green hydrogen, produced via water electrolysis using renewable sources, such as solar or wind energy, stands as a pivotal resource with versatile applications. It serves as a key ingredient for electricity generation through fuel cells, while also being a valuable component in the production of value-added chemicals, such as methanol, via hydrogenation.[1] The hydrogen evolution reaction (HER) represents the cathodic half of the overall water splitting process and a wide array of hydride-forming transition metal complexes have been reported to accelerate this transformation.[2–13] These homogeneous electrocatalysts have been explored in great detail to understand the electronic and structural factors that control proton-coupled electron transfer (PCET) processes underlying HER. For example, Blakemore and others performed extensive mechanistic studies of HER catalysis by $[Cp^*(bpy)Rh^{III}\text{-}Cl]^+$ and other analogous complexes.[14–17] The authors found that $Cp^*Rh^{I}(bpy)$, electro-generated via a two-electron, Rh-centered reduction of the precursor complex and subsequent loss of the labile halide ligand, represents a key catalytic intermediate. The basicity of $Cp^*Rh^{I}(bpy)$ controls formation of the protonated hydride form, $[Cp^*(bpy)Rh^{III}\text{-}H]^+$, and the kinetics of the subsequent HER reactivity. Protonation of $Cp^*Rh^{I}(bpy)$ was found to occur only in the acidic region and the initial protonation site is the Rh-center which forms $[Cp^*(bpy)Rh^{III}\text{-}H]^+$ intermediate.[18–22] Interestingly, this kinetic product is

short-lived, and was shown to tautomerize into a thermodynamically more stable ligand-protonated [Cp*-H(bpy)Rh^{I}]$^{+}$ form, which was characterized using single-crystal X-ray diffraction.[20,22] The HER activity is intimately connected with the energetics and the stereochemistry of this protonation step. For example, the two-electron reduced Cp*Rh^{I}(bpy) did not protonate at pH < 6,[18] which has been explored to catalyze the reduction of other substrates, such as NAD^{+}.[18,23–25] Here, the hydride transfer reactivity is dependent on the basicity of the Cp* ligand (Cp*H pK_a = 9), suggesting atypical non-innocence of Cp* and unique cooperativity between Rh and Cp* in proton and electron accumulation.[18]

When molecular electrocatalysts are anchored onto an electrode surface through covalent bonds, such as those formed using ortho-quinone[26] or diazonium[27] functionalization methods, they encounter electric fields at the interface between the electrode and the electrolyte.[26,28–40] These electric fields have a profound effect on the outer-sphere electron transfer (ET) processes. For instance, research led by the Surendranath group has demonstrated that outer-sphere electron transfer (ET) processes, like the oxidation from Ru(II) to Ru(III), can be completely inhibited.[33] This happens due to the cancelation of the electric field effects on electrochemical potentials of charge carriers and redox-active moieties. Moreover, the Mirkin group's findings suggest that when the redox-active part of a molecule is positioned at an intermediate distance within the electric double layer, the charge carriers, redox-active sites, and substrate molecules experience varying electric field intensities.[41–44] This variation in electric field strength within the electric double layer adds an extra "push" for ET between the redox sites and the substrates, which enhances redox catalysis. The influence of electric fields also extends to the electron-coupled bond forming/breaking steps,[37–39] as well as the catalytic processes mediated by the surface-immobilized species.[28,34–36,40] For example, when a molecular Rh-based HER catalyst was attached to the carbon electrode, its electrocatalytic behavior was drastically different from that observed for its homogeneous analog ([Cp*(bpy)Rh^{III}-Cl]$^{+}$): while the homogeneous catalyst was active only in a narrow range of pH values, the immobilized analog maintained its catalytic performance over the entire experimentally accessible pH window.[33,35,36] Here, the electric fields experienced by the immobilized catalyst led to superior catalytic performance by preventing the undesired outer-sphere ET processes.

Non-covalent immobilization strategies have also been explored, often for planar macrocycle complexes, such as metal porphyrins or phthalocyanines.[45–49] Again, the immobilized

catalysts were found to exhibit different electrochemical behavior from that observed for their homogeneous analogs. For example, electrocatalytic CO_2 reduction by Co-phthalocyanine (CoPc) adsorbed onto conductive carbon supports was found to exhibit drastic differences in product selectivity, forming either only CO or a CO/CH_3OH mixture, depending on the subtle and poorly understood differences in the preparation of these molecule/electrode hybrid materials.[50–54] A recent study explored the effect of the carbon support on the catalytic performance and observed differences in reactivity when CoPc was adsorbed onto carbon nanotubes (CNT) with different diameters. The diverging behaviors were assigned to the increased macrocycle strain imparted on CoPc by differing carbon nanotube curvatures, resulting in differences in *CO binding energies.[55] In addition to these structural factors, the adsorbed macrocycles are positioned in intimate proximity to conductive CNT which results in its the electrochemical behavior being further modulated by the large electric fields experienced at the electrode/electrolyte interfaces.[46]

Our group investigates graphene nanoribbons (GNRs) for immobilization of molecular catalysts to the electrode surface using noncovalent interactions (Scheme 1). These GNRs are synthesized using bottom-up synthetic methodology first reported by Sinitskii and co-workers.[56] In a previous study, we took advantage of the redox-active nitrogen functionality to investigate the electrochemical behavior of immobilized GNRs.[57] We found that the PCET of immobilized GNRs deviated from that observed for a homogeneous model compound, bipyrimidine (**bpm**), indicating that the interfacial electric fields modulate the electrochemical behavior of GNRs. In this study, we investigated the electrochemical behavior of GNR 2D nanosheets (**GNR-2DNS**) and Rh-coordinated GNR 2D nanosheets (**RhGNR-2DNS**) and its activity towards the HER. We demonstrated that **GNR-2DNS** strongly couple to GC electrodes and that **RhGNR-2DNS** do not. However, **RhGNR-2DNS** was an active electrocatalyst for the HER and performed in a broader set of aqueous pH conditions than its molecular analogs. PCET-hosting bipyrimidine-based ligands were shown to dramatically alter the activity of Rh sites and provide **RhGNR-2DNS** the improved catalysis.

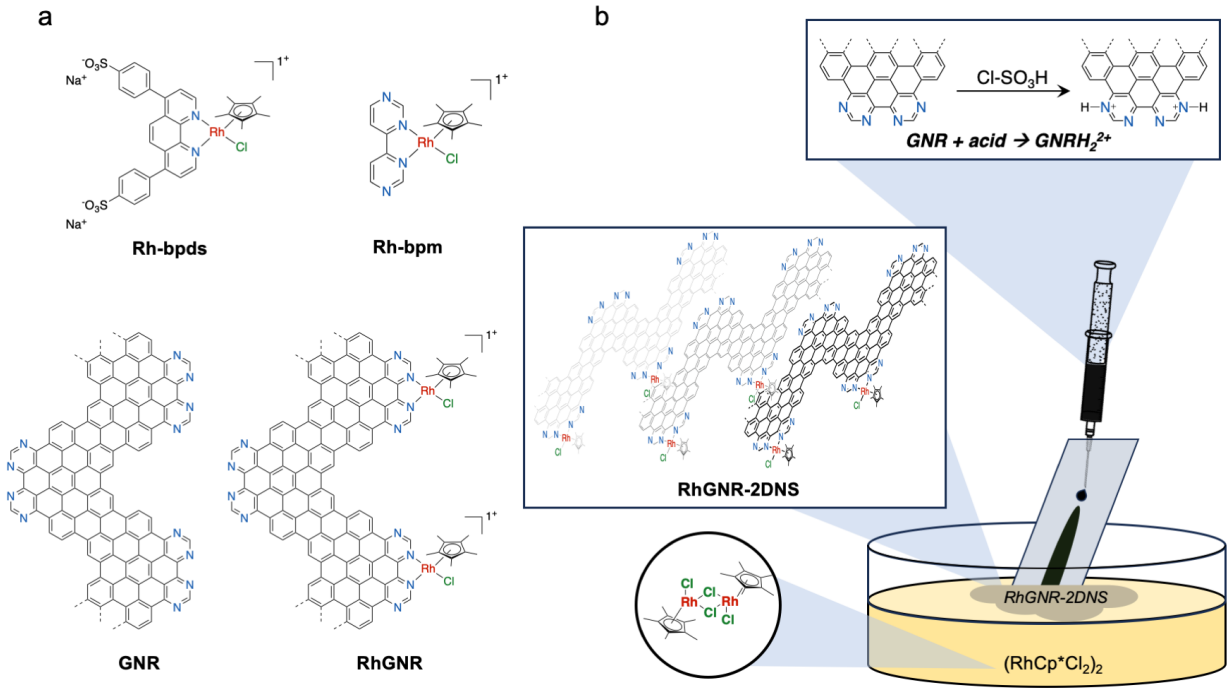

Scheme 1. a) Structures of the molecular model compounds (**Rh-bpds** and **Rh-bpm**) and GNR samples (**GNR** and **RhGNR**). b) Liquid-air interfacial preparation of **RhGNR-2DNS**.

Results and Discussion

Preparation and Characterization of RhGNR-2DNS. The GNRs were prepared following a procedure published by Sinitskii (Scheme S1).[56] The synthesis involved three principal steps: 1) Diels-Alder cycloaddition and decarbonylation step, which generated the dibrominated monomer 8;[58] 2) Yamamoto C-C coupling of the monomer to produce the non-planarized oligomer 9; 3) $FeCl_3$-mediated cyclodehydrogenation of oligomer 9 to produce the planar GNRs. Full synthetic details and characterization of the GNRs using solid-state NMR, Raman spectroscopy, transmission electron microscopy and X-ray photoelectron spectroscopy (XPS) has been reported previously.[57] **GNR-2DNS** and **RhGNR-2DNS** were prepared on glassy carbon (GC) electrodes according to a modified Langmuir-Schaefer (LS) deposition process (Scheme 1b).[59,60] This technique leveraged the GNR's hydrophobicity and tendency to minimize solvent interactions by self-assembly into dense, π-stacked monolayers when introduced to a polar solvent, i.e. deionized H_2O. GNR powder was first dissolved in chlorosulfonic acid via the protonation of N-sites and this solution was slowly introduced onto the surface of the aqueous solution containing the

precursor complex, pentamethylcyclopentadienyl rhodium(III) chloride dimer $(RhCp^*Cl_2)_2$. The neutralization of protonated GNRs resulted in self-assembly at the water/air interface, generating **RhGNR-2DNS** that were visible to the naked eye and reached widths in excess of 2 cm. **GNR-2DNS** films were prepared in the same way, in the absence of the Rh-based precursor.

Scanning electron microscopy (SEM) images demonstrated the uniformity of both **GNR-2DNS** and **RhGNR-2DNS**, with single domain sizes reaching up to 1 mm in length (Figure S1). Close-up atomic force microscopy (AFM) images revealed a roughly 2 nm step height from the Si/SiO_2 substrate to our prepared film (Figure S2). The measured distance corresponds to the width of our chevron-type GNR and agrees well with what has been reported previously for **GNR-2DNS**.[60] AFM analysis suggests the **GNR-2DNS** and **RhGNR-2DNS** films self-assemble in an "edge-on" configuration at the liquid-air interface and that orientation was retained once transferred to a substrate. High resolution X-ray photoelectron (XPS) spectra in the N 1s and Rh 3d regions were also collected on **GNR-2DNS** and **RhGNR-2DNS** samples to gain deeper insight into the interaction between GNR and Rh. Based on the fitting of experimental N 1s data (Figure S3a), **GNR-2DNS** features predominant peaks at 398.8 and 401.3 eV, which have previously been assigned to imine-like nitrogen sites in weak and strong electronic communication with the electrode, respectively.[57,61,62] An additional feature was present at 400.3 eV which came from native nitrogen species present on commercial carbon electrodes.[63] **RhGNR-2DNS** featured similar peaks as GNR, with an additional feature at 399.9 eV which we assigned to the imine-N sites on Rh-coordinated GNRs. The ~1 eV shift to higher binding energies upon Rh coordination results from σ donation to Rh from pyrimidine units of GNR. The Rh 3d spectra of **RhGNR-2DNS** exhibited the $3d_{5/2}$ and $3d_{3/2}$ doublet at 309.7 and 314.3 eV, respectively, which is consistent with Rh(III) oxidation state (Figure S3b).[64] Importantly, both the $3d_{5/2}$ and $3d_{3/2}$ peaks were fit with a single gaussian function, indicating a single Rh speciation in **RhGNR-2DNS**.

Synchrotron-based X-ray absorption spectroscopy (XAS) at the Rh K-edge was utilized to examine the molecular structure of **RhGNR-2DNS**. To aid the data analysis, the XAS measurements were also performed on a model compound **Rh-bpds** (structure shown in Scheme 1, while the synthesis and characterization is summarized in the SI). Estimates of the Rh oxidation state in **Rh-bpds** and **RhGNR-2DNS** were done by comparison of the absorption edge in the X-ray absorption near edge spectrum (XANES) region, relative to a series of Rh standards (Table S8 and Figure S16a and b). Both samples were assigned to be in the Rh(III) oxidation state. To gain

atomic-level insight into the local structure around Rh in **Rh-bpds** and **RhGNR-2DNS**, extended X-ray absorption fine structure (EXAFS) data were fit using a crystal structure of a similar bipyridine-ligated RhCp* complex reported in the literature (Figure S17).[65] EXAFS fitting of **Rh-bpds** and **RhGNR-2DNS** was performed using the Artemis software package.[66] Our best fits featured a total of eight atoms in the first coordination shell of Rh. This included a combination of seven N (imine sites) or C atoms (Cp* ring) and one Cl atom (chloride ligand). Average bond lengths for Rh–N/Rh–C and Rh–Cl were within 0.02 Å of the reported crystal structure and are presented in Tables S9, S10 and S11. These experimental results support our assignment of the **RhGNR-2DNS** structure as is shown in Scheme 1, involving a coordination of the Rh complexes to imine-N sites of GNR.

Electronic properties of molecular analogs (**bpm** and **Rh-bpm**) and film samples (**GNR-2DNS** and **RhGNR-2DNS**) were studied using combined spectroscopic and computational approaches. The UV/Vis absorption spectra of **GNR-2DNS** and **RhGNR-2DNS**, collected using photothermal deflection spectroscopy (PDS), are shown in Figure 1a. For comparison, Figure 1a also shows the solution-based transmission spectra of the model compounds **bpm** and **Rh-bpm** (the structure of **Rh-bpm** is shown in Scheme 1, while the synthesis of **Rh-bpm** is summarized in the SI). The experimental UV-Vis spectrum of **bpm** exhibits intense absorption at 270 nm which is consistent with the computationally predicted π–π* transition at 261 nm (Figure 1b, computational details are summarized in Section 5 of the Supplementary Information). **Rh-bpm** has similar high energy absorption features at 270 nm and an additional broad absorption band in the 350 and 500 nm range. This low energy absorption was also predicted in the calculated spectrum of **Rh-bpm**, as shown in Figure 1b. Based on the molecular orbitals involved in the lowest-energy transition of **Rh-bpm** (Figure S5), we assigned the broad absorption band to the ligand-to-ligand charge transfer (LLCT) transitions with significant charge transfer from Cl^- to the bpm and Cp* ligands ($Cl^- \rightarrow$ bpm and Cp* LLCT state), and our assignment is consistent with the previous report.[67]

The PDS of **GNR-2DNS** showed a broad absorption in the 400-700 nm range (Figure S4a), which is consistent with the UV/Vis absorption spectrum reported for the analogous GNR in solution.[68] Likewise, the calculated spectrum of a model compound with reduced size (**Flake**, structure shown in Figure S6) exhibits low energy transitions at 462 and 478 nm. The lowest energy transition in the **Flake** is assigned to the π–π* transition with a significant charge transfer

character to the bipyrimidine unit, as illustrated by the molecular orbitals involved in the transition (Figure 1c).

The PDS of **RhGNR-2DNS** was qualitatively similar to that of **GNR-2DNS** (Figure 1a). A small degree of red shift was observed in the absorption maximum, which may arise due to the presence of Rh-coordinated moieties. The experimentally observed red-shift was not as significant as the calculated shift for the **Rh-Flake** (structure shown in Figure S6) model compound, where the Rh-coordination resulted in the appearance of a new band at 531 nm (Figure 1b). The molecular orbitals for the three lowest energy transitions in **Rh-Flake** are shown in Figure 1c and indicate that the first two excited states arise due to ligand-centered transitions, while the third excited state reflects LLCT character similar to **Rh-bpm**. Thus, it appears that the increased conjugation of the ligand from bpm to Flake increases the contribution of the ligand-centered excited states and this effect is expected to be even more pronounced as one goes from **Rh-Flake** to **RhGNR**, since the ligand-centered transitions decrease in energy with the introduction of additional monomer units.[68] Given, this reasoning, we conclude that the electronic spectroscopy of **RhGNR-2DNS** is dominated by the π–π* transitions located on the GNR, making the spectra less sensitive to Rh-coordination.

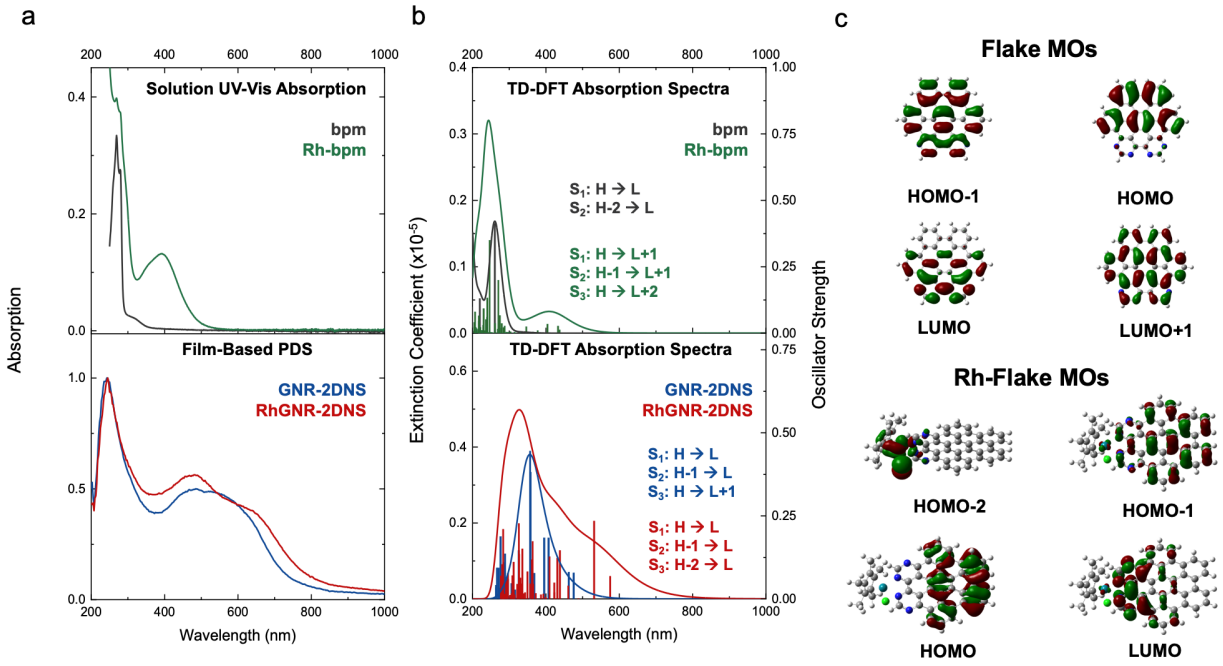

Figure 1. a) Absorption spectra of **bpm**, **Rh-bpm** (top panel, spectra collected as solution-based UV-Vis absorption), **GNR-2DNS** and **RhGNR-2DNS** (bottom panel, spectra collected by photothermal deflection spectroscopy (PDS) on deposited films). b) TD-DFT spectra of **bpm**, **Rh-bpm**, **Flake** and **Rh-Flake**. Vertical lines represent predicted electronic transitions. c) Orbitals involved in the lowest energy electronic transitions shown with representative charge distribution.

Ligand-centered reduction. GNR-2DNS films deposited on GC electrodes were redox-active and displayed a single, chemically reversible feature in the +0.02 to -0.70 V vs NHE range (Figure 2). This redox-feature shifted to more negative potentials with increasing pH, indicating that the process involved proton-coupled electron transfer (PCET). Similar behavior was observed for a homogeneous model compound, **bpm** (Figure 2 and Ref 57), and we assigned this signal to a proton-coupled reduction of the bipyrimidine moieties of both **bpm** and **GNR-2DNS** to form the hydrogenated species shown in Scheme 2. The cathodic-to-anodic peak-to-peak separation observed in **GNR-2DNS** varied between 30-50 mV, indicating a small kinetic barrier associated with the observed charge transfer process and strong electronic coupling of **GNR-2DNS** with the glassy carbon electrode. In our previous study,[57] we observed similar "strongly coupled" responses for GNR samples drop-casted onto the electrode surface. However, in the previous study, electrochemical pre-treatment was required to disperse the "weakly-coupled" GNR aggregates and form GNR monolayers in strong electronic communication with the electrode. In this study, the response of the "strongly coupled" GNRs was obtained for as-deposited samples, without the need for additional electrochemical pre-treatment.

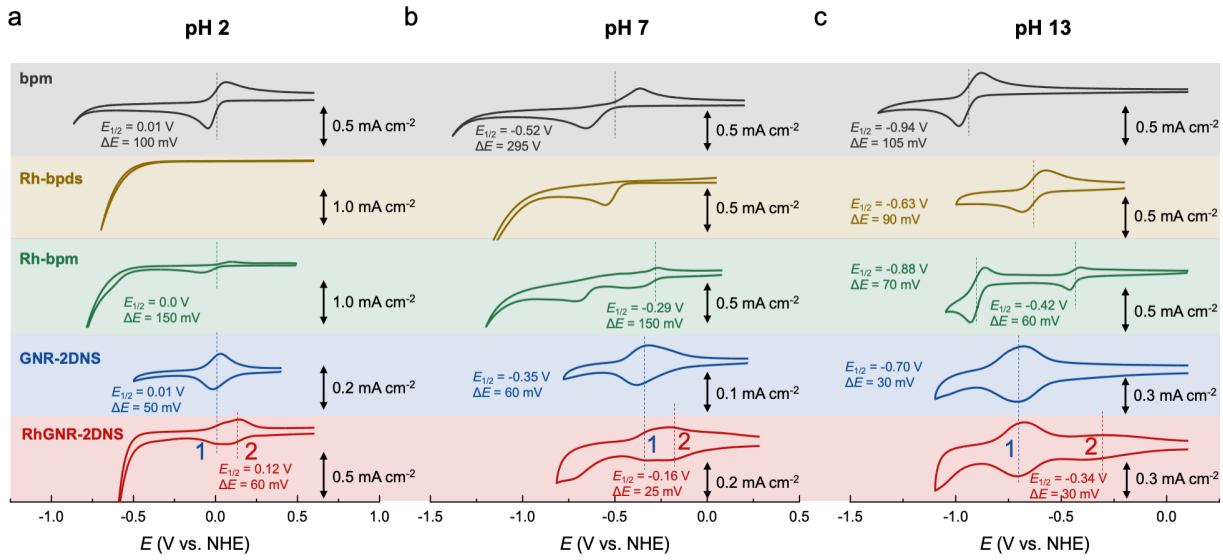

Figure 2. CVs of **bpm** (gray), **Rh-bpds** (gold), **Rh-bpm** (green), **GNR-2DNS** (blue) and **RhGNR-2DNS** (red) recorded in 0.1 M sodium phosphate solutions at pH a) 2, b) 7 and c) 13. **RhGNR-2DNS** samples feature two cathodic features which are assigned to 1) bipyrimidine unit reduction on the un-coordinated **RhGNR-2DNS** sites (blue text) and 2) bipyrimidine unit reduction on Rh-coordinated **RhGNR-2DNS** sites (red text). CVs are referenced vs. NHE and were recorded at 100 mV/s scan rates on glassy carbon working electrodes with an Ag/AgCl and Pt wire reference and counter electrode, respectively.

The charge associated with the bipyrimidine reduction peaks in **GNR-2DNS** was derived by integrating the cathodic CV peak across the entire pH region which gave rise to an average value of $6.47 \cdot 10^{-5}$ C cm^{-2}. This value agreed well with the charge expected for a two-electron reduction of a monolayer of vertically aligned **GNR-2DNS**, ($4.86 \cdot 10^{-5}$ C cm^{-2}, Supporting Information Section 4). The vertical alignment of **GNR-2DNS** films is also consistent with AFM data collected on the same electrode (Figure S2). The number of surface layers covering the electrode was tuned by increasing the concentration of GNR/CSA precursor solutions or increasing the number of LS deposition steps (Figure S10). In multi-layer **GNR-2DNS** films, a secondary CV feature appeared with significantly larger (130 mV) cathodic-to-anodic peak separations (Figure S10c), which indicates increased kinetic sluggishness associated with the PCET process in thicker samples. For simplicity, we limited our investigation to the mono-layer samples for all follow-up GNR experiments reported here.

The $E_{1/2}$ of the bipyrimidine reduction feature in **GNR-2DNS** shifts to a more negative value with increasing pH, as illustrated in the Pourbaix diagram in Figure 3b (light blue trace). This pH-dependence is consistent with a PCET process and similar behavior is observed for the homogeneous model compound **bpm** (Figure 3a, gray trace). However, the Pourbaix slopes for **bpm** and **GNR-2DNS** are significantly different. In the case of **bpm**, three regions with differing Pourbaix slopes were observed, and linear fitting of the data revealed three distinct regions of pH-dependence for **bpm** with a differing number of protons transferred in each region (Figure 3, Scheme 2). The fitting of our experimental data gives a value for E^0_{PCET}(**bpm**/**bpmH$_2$**) = +0.25 V and the pK$_a$ values of pK$_{a,1}$ (**bpmH$_4^{2+}$** → **bpmH$_3^+$** + H$^+$) = 4.2 and pK$_{a,2}$ (**bpmH$_3^+$** → **bpmH$_2$** + H$^+$) = 8.0 (Section S4 of the Supplementary Information). The E$_{1/2}$ and pK$_a$ values are in qualitative agreement with DFT calculated E^0_{PCET}, pK$_{a,1}$ and pK$_{a,2}$ values of +0.43 V vs NHE, 0.6 and 10.3, respectively (Section S5 of the Supplementary Information).

To confirm our assignment of three distinct pH regions in the Pourbaix diagram of **bpm**, we performed UV-Vis absorption spectroelectrochemistry (SEC) measurements on solutions of **bpm** at three representative pHs (2, 7 and 13, Figure S11a, b and c). In all solutions, at applied potentials more negative than the **bpm** reduction potential, a new absorption signal emerged concomitant to the loss of the main **bpm** absorption feature at 271 nm, which indicated the presence of a new species. The new absorption signal was red-shifted relative to the main **bpm** absorption and appeared at 297, 313 and 322 nm in solutions of pH 2, 7 and 13, respectively. These values agree excellently with DFT-computed absorption spectra for the **bpmH$_4^{2+}$**, **bpmH$_3^+$** and **bpmH$_2$** species which show absorption centered at 296, 310 and 322 nm, respectively (Figure S11d). Our assignment for **bpm** electrochemistry was thus slightly modified from our original work, where only two distinct pH regions were identified.[57] The updated model presented here is more consistent with additional theoretical modeling and SEC results.

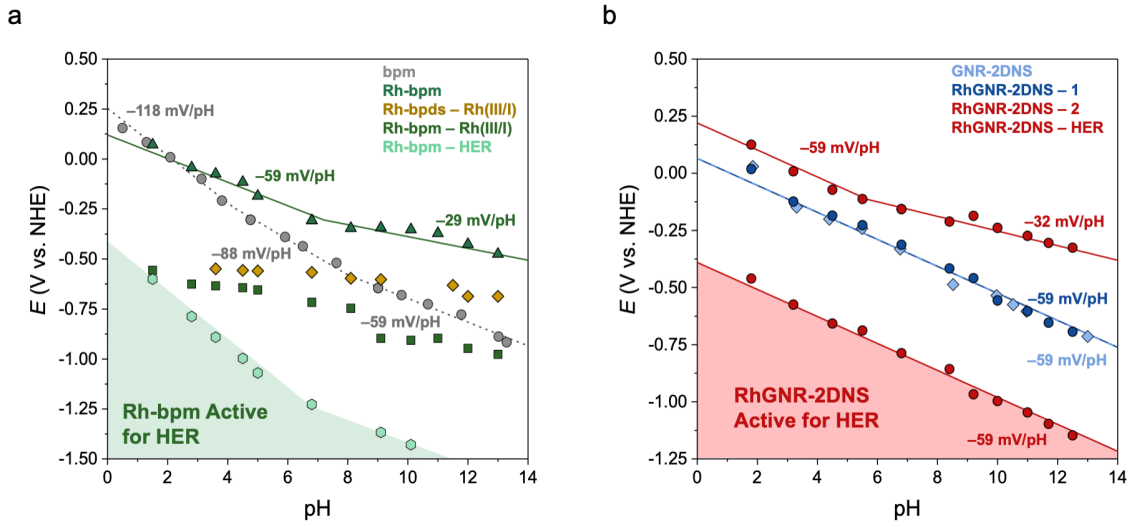

Figure 3. Pourbaix diagrams of all a) molecular analogs (**bpm**, **Rh-bpm** and **Rh-bpds**) and b) GNR-based (**GNR-2DNS** and **RhGNR-2DNS**) samples investigated in this study. Positions for the bipyrimidine-centered PCET, Rh-centered reduction and HER onset are denoted on each panel. To account for the discrepancies in $E_{Rh(III/I)}$ values introduced by the chemically irreversible Rh(III/I) reduction in acidic and neutral solutions, we recorded only the cathodic Rh(III/I) feature. The assigned slopes in the Pourbaix diagram were determined through linear regression fitting assuming a net ***m*** proton, ***n*** electron transfer PCET process. The fraction of the interfacial potential experienced (***f***) was assumed to be 0 for the molecular model compounds (**bpm** and **Rh-bpm**).

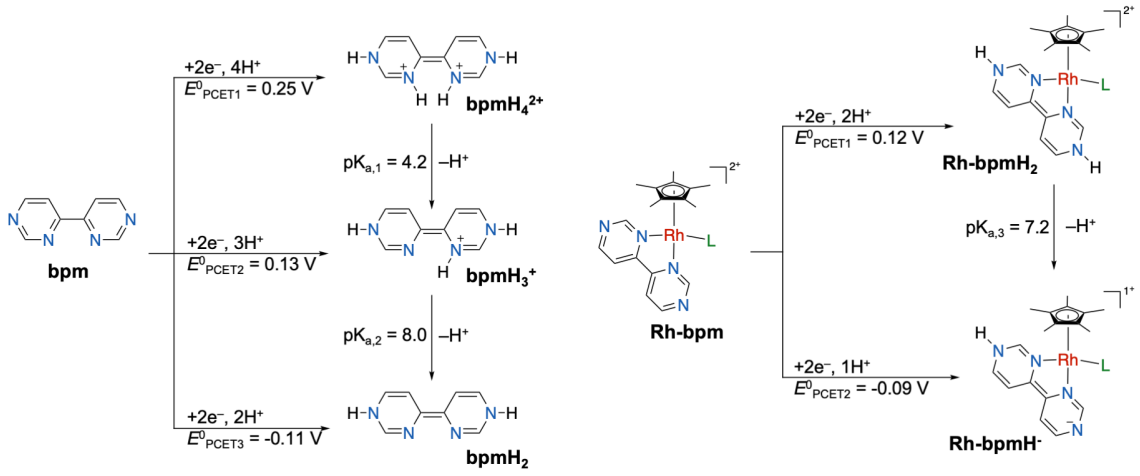

Scheme 2. Representative structures for all PCET transitions assigned in the Pourbaix diagrams of Figure 3.

The Pourbaix diagram for **GNR-2DNS** is significantly different from **bpm** – only a single slope of –59 mV per pH unit was observed throughout the entire pH region (Figure 3). Such an intriguing change in the Pourbaix slope is fully consistent with the effect that interfacial electric fields are expected to exert on **GNR-2DNS** immobilized at the electrode/electrolyte interface (Figure 4a). To model the effect of interfacial potential on PCET, we derived an expression which predicted how Pourbaix slopes change with the interfacial potential experienced by a redox-active PCET group. For this purpose, we adopted a model similar to what has been used previously to model proton transfer and PCET processes in monolayer films that contain acid-base groups.[37,69,70] We assume that the redox-active group experiences a fraction of the overall potential ($\Psi_M - \Psi_S$) that is formed at the electrode/electrolyte interface. This fraction is defined by a parameter, ***f***, whose values range from 0 to 1. Parameter ***f*** adopts a value of zero for PCET occurring in the bulk solution and a value of 1 for PCET occurring at the electrode surface. We then derived the expression that related how Pourbaix slopes changed with parameter ***f*** (Section 7 of the Supporting Information). The dependence is displayed in Figure 4a and shows that the Pourbaix slope depends on parameters ***m*** (number of protons transferred during PCET), ***n*** (number of electrons transferred during PCET) and ***f***. Figure 4b plots the effect that the interfacial potentials have on the Pourbaix slopes. If PCET occurs in the bulk solution, the parameter ***f*** becomes zero and the Pourbaix slope simplifies to the well-known values of –59·**m**/**n** mV per pH unit (at room temperature). This PCET slope has been very useful in studies of PCET in homogeneous systems, as it reports on the relative ratio **m**/**n**, providing information on the number of electrons and protons transferred during PCET.[36,57,71] In our case, we used the slopes observed for **bpm** to assign three PCET processes taking place in three pH regions: **bpm/bpmH$_4^{2+}$** interconversion in the acidic region (**m**=4 & **n**=2, slope of –118 mV per pH unit), **bpm/bpmH$_3^{+}$** interconversion in the neutral pH range (**m**=3 & **n**=2, slope of –88 mV per pH unit) and **bpm/bpmH$_2$** interconversion in the basic region (**m**=2 & **n**=2, slope of –59 mV per pH unit, Scheme 2).

Interestingly, as the ***f*** parameter increases to a value of 1, Pourbaix slopes for all PCET processes, regardless of ***m*** or ***n***, merge into a unique value of –59 mV per pH unit. In other words, when the redox-active PCET group is adsorbed directly on the electrode surface, information regarding the number of protons and electrons transferred during PCET disappears from the Pourbaix slope. For **GNR-2DNS**, a single slope of –59 mV per pH unit has been observed in all

pH-regions, indicating that the bipyrimidine groups experience the full potential at the electrode surface, confirming our assignment of strong electronic coupling. Given the model presented in Figure 4, we can no longer identify how many protons are transferred per each electron, since this information is absent from the Pourbaix slope expression.

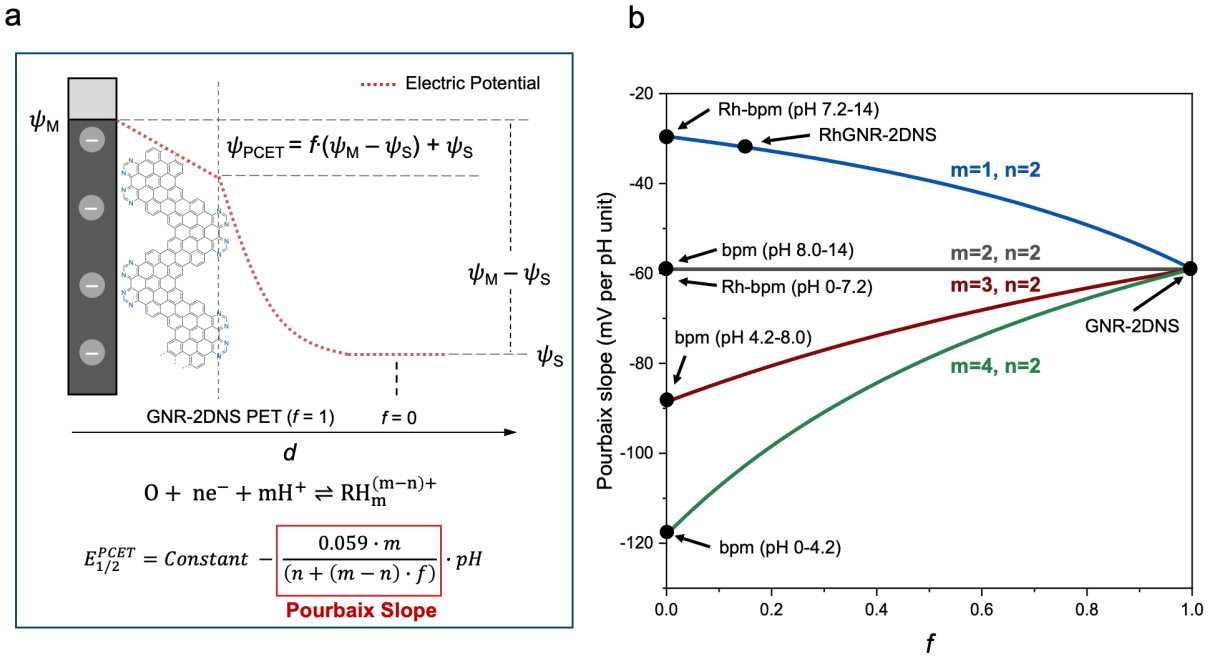

Figure 4. a) Illustration of the driving forces for electron transfer. The superimposed **GNR-2DNS** in its vertically aligned configuration experiences the full interfacial potential at the electrode. b) Plot showing the predicted Pourbaix slopes for an **m** H^+:**n** e^- PCET processes based on ***f***. Data points collected for the model compounds (**bpm** and **Rh-bpm**), **GNR-2DNS** and **RhGNR-2DNS** are plotted.

Unlike the behavior of **GNR-2DNS**, CVs of **RhGNR-2DNS** films reveal two reversible, and partially overlapping, features across the entire aqueous pH region (Figure 2, red traces). We assigned these two reduction features to PCET at bipyrimidine moieties that are either un-coordinated (feature **1**, peaks that appear at the same potential as **GNR-2DNS** at all pHs) or Rh-coordinated (feature **2**, peaks appear at more positive potentials, due to the electron-withdrawing σ-acceptor nature of Rh-atoms). $E_{1/2}$ of the two features were separated by ~100 mV to up to 400

mV in acidic and basic solutions, respectively. The relative peak area integrations of the two features suggest that ~40% of redox-active bipyrimidine units are coordinated with Rh-centers.

Both features, **1** and **2**, showed discernible non-zero Pourbaix slopes which is indicative of PCET at bipyrimidine units (Figure 3b). Feature **1** exhibits the same behavior as **GNR-2DNS**, with a single –59 mV per pH unit slope across the entire pH range, which is consistent with the PCET involving strongly coupled PCET moieties, as discussed above. Interestingly, the Rh-coordinated feature **2** exhibits a different behavior in the basic region (pH = 5.7 – 14), where the Pourbaix slope of –32 mV per pH unit was recorded. The observed Pourbaix slope is quite similar to that of homogenous model compound **Rh-bpm**, which exhibits a –59 mV slope in the acidic region (pH = 0 – 7.2) and a –29 mV per pH unit slope in the basic region (pH > 7.2). Different Pourbaix slopes observed in **Rh-bpm** and **RhGNR-2DNS** are assigned to PCET processes that involve two electrons and two protons in the acidic region (m = 2, n = 2) to make **Rh-bpmH$_2$** fragments. The reactivity switches to a two-electron, one-proton PCET process in the basic region (m = 1, n = 2) to make **Rh-bpmH$^-$** fragments as shown in Scheme 2. The fitting of our experimental data gives E^0_{PCET} values of +0.12 and +0.22 V for the two-proton, two-electron conversion of **Rh-bpm** and Rh-coordinated GNR units (**RhGNR-2DNS** feature **2**), respectively. The fitting was also used to extract pK_a values for dissociation of a single proton at the reduced bipyrimidine sites (**Rh-bpmH$_2$** $\rightarrow$ Rh-**bpmH**$^-$ + H$^+$ or Rh-GNRH$_2$ $\rightarrow$ Rh-GNRH$^-$ + H$^+$, p$K_{a,3}$). p$K_{a,3}$ values of 7.2 and 5.7 were observed for the **Rh-bpm** and **RhGNR-2DNS**, respectively, which agreed qualitatively with DFT-calculated p$K_{a,3}$ values (Tables S3, S5 and S7).

Similar to **bpm**, SEC measurements were performed on solutions of **Rh-bpm** at pHs 2, 10 and 13 to confirm our Pourbaix diagram assignments (Figure S12a, b and c). At pH 2, under –0.3 V applied potential, the main **Rh-bpm** absorption feature at 288 nm decreased in intensity while a new feature centered at 321 nm appeared which agrees excellently with the computed absorption spectra for **Rh-bpmH$_2$** (Figure S12d) and confirms it as the product of **Rh-bpm** reduction from pH 0 – 7.2. In basic solutions (pH 10 and 13) under applied cathodic potentials, the only observed spectral change was a decrease to the intensity of the **Rh-bpm** absorption. The **Rh-bpm** signal intensity was recovered when anodic potentials were applied. After performing measurements at constant cathodic potentials, the working electrode was removed from solution and rinsed thoroughly. Subsequent CVs recorded in fresh electrolyte solutions showed the presence of an anodic oxidation feature at –0.21 V vs. NHE (Figure S9). Combined together with the signal

intensity losses observed in SEC measurements, we concluded that within the basic pH regions (pH > 10), ligand-centered reduction of **Rh-bpm** results in deposition on the electrode surface. We expect deposition happens as a result of formation of the **Rh-bpmH**$^{-}$ fragment with anionic **bpmH**$^{-}$ ligand.

The differing Pourbaix slopes of features **1** and **2** in **RhGNR-2DNS** imply that the two functional groups experience different interfacial potentials. While uncoordinated **GNR-2DNS** are strongly coordinated to the electrode surface and experience the full fraction (f = 1) of the interfacial potential, the Rh-coordinated **RhGNR-2DNS** behaves like a molecule in the bulk solution, indicating only weak effects of interfacial electric fields on the Rh-coordinated site (Figure 4b). These results indicate that there is some degree of structural rearrangement within 2D nanosheets that accompanies Rh-coordination. This structural rearrangement appears to push the Rh-coordinated bipyrimidine moieties away from the electrode surface, reducing the potential experienced by the moiety.

Rh-centered reduction. Rh-bpds and its analogs are well-studied HER catalyst in acidic aqueous media.[14–16,19,21,22] Here, **Rh-bpds** served as a molecular analog for a comparative study of the Rh-centered redox chemistry. Our electrochemistry matched well with previous literature reports.[35] At pH 1, no reversible features were observed in the CV but there was a large cathodic current resulting from Rh-mediated HER which picks up to a catalytic onset current of 1 mA cm^{-2} at -0.52 V (Figure 2a). At pH 7, we observed a chemically irreversible Rh pre-feature at -0.60 V, followed by HER onset at -1.17 V (Figure 2b and S6b). The pre-feature was assigned to a Rh-centered, 2e^{-} reduction followed by protonation of the nascent Rh(I) intermediate to form Rh(III)–H. By pH 9.1 and beyond, we observed no HER current apart from what was present from the bare glassy carbon electrode (Figure 5a and Figure S6) and by pH 13 a reversible 2e^{-} Rh(III/I) reduction at -0.68 V was observed (Figure 2c). The $E_{Rh(III/I)}$ values are pH-independent while the HER activity has a clear dependence on the solution acidity (Figure S7). The HER activity dissapears at pHs higher than 8.1 because **Rh-bpds** no longer possessed the basicity required to generate the requisite Rh(III)–H intermediate necessary to host HER.[18,35]

Rh-centered reduction of the **Rh-bpm** model behaved similarly to **Rh-bpds** with two major differences: First, Rh(III/I) reduction ($E_{Rh(III/I)}$) appeared at more negative potentials for **Rh-bpm** than **Rh-bpds** (Figure 3a and S6). This shift in the potential is consistent with the increased electron-density of reduced bipyirimidine ligands formed at potentials more positive than $E_{Rh(III/I)}$

(Figure 2). DFT calculations support this conclusion and predicted the $E_{Rh(III/I)}$ values to be ordered by **Rh-bpm** > **Rh-bpy** > **Rh-bpmH$_2$** > **Rh-bpmH$^-$** (Table S6). Secondly, we observed an extension of the pH window (up to pH 10.1) for which **Rh-bpm** was active for HER (Figure 3 and S6). This increased pH range over which **Rh-bpm** retained its HER activity was assigned to the increased basicity of the 2e$^-$-reduced Rh(I) intermediate, forming protonated Rh(I)Cp*–H and Cp*Rh(III)-H species that are essential for catalytic turnover. Our DFT evidence showed that the reduced **bpmH$_2$**/**bpmH$^-$** ligands destabilize the Rh-centered HOMO of the 2e$^-$-reduced Rh(I) intermediates, and thus dramatically increase their basicity and lead to an extended window of HER activity (Figure S13, Table S6). Because of the beneficial effects from the "responsive", PCET-hosting **bpm** ligand, the **Rh-bpmH$^-$** was predicted to maintain HER activity well outside the aqueous pH window – predicted pK_a's for the Rh(III)–H and Rh(I)Cp*–H species were 26.6 and 31.7, respectively. We postulate that the reason for the loss of HER activity in the basic region is not associated with the low basicity of Rh(I) species (as is the case for **Rh-bpds**), but with the aggregation of **Rh-bpmH$^-$** species we described in the previous section. The exact nature of the aggregate is outside the scope of this study, but clearly the ligand-centered reduction to form anionic **bpmH$^-$** triggered its formation, resulting in electrode passivation and termination of HER activity (see Section S4 of the Supplementary Information for more detail).

Voltammetry of **RhGNR-2DNS** showed no signature of Rh-centered reduction, however it did show activity for HER which was maintained throughout the entire aqueous pH window (Figure 5b). The observed onset of HER (taken as potential where TOF = 1 s^{-1}) shifted with pH by –59 mV per pH unit. This stands in contrast to studies on our molecular analogs whose catalytic activity was confined to pHs ≤ 10.1. It appears that the immobilization of Rh-centers onto the electrode surface enhances the electrocatalytic performance of **RhGNR-2DNS** toward HER. Similar behavior has been observed by Surendranath on Rh-modified carbon electrodes and was assigned to the electric fields experienced by the Rh-center.[35] In our case, such field effects are not likely to influence catalytic behavior of **RhGNR-2DNS**, since the Pourbaix analysis described in the previous section indicated that the Rh-moieties experience negligible interfacial potentials (Figure 4). Thus, the observed electrocatalytic enhancements in **RhGNR-2DNS** are associated with a different mechanism.

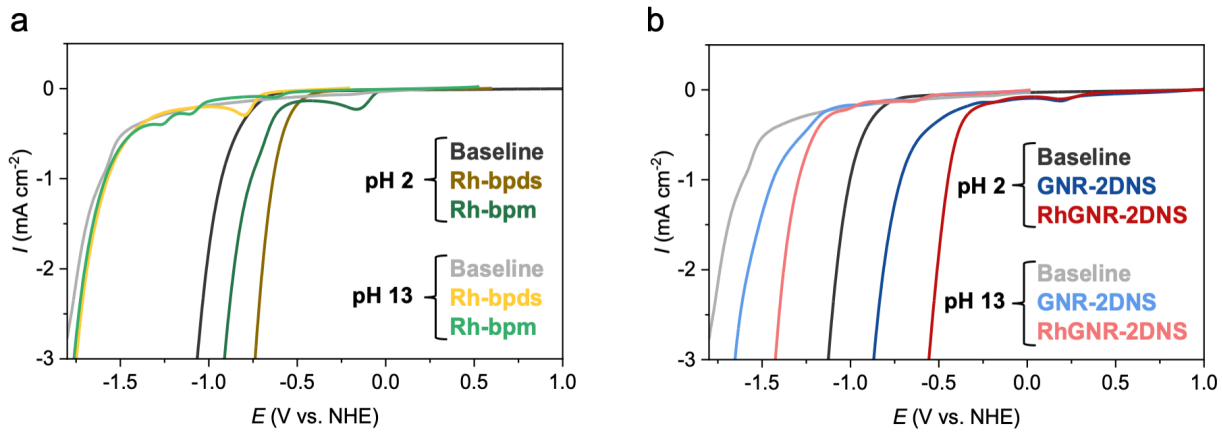

Figure 5. Linear sweep voltammograms (LSVs) recorded at pH 2 and 13 for all a) model compounds and b) GNR-based samples. LSVs are referenced vs. NHE and were recorded at 100 mV/s scan rates on glassy carbon working electrodes with an Ag/AgCl and Pt wire reference and counter electrode, respectively.

To investigate the mechanism of Rh-mediated HER in **RhGNR-2DNS** samples, we performed in situ grazing incidence X-ray absorption near edge structure (GI-XANES) measurements (Figure 6). Comprehensive details of these measurements can be found in Section 6 of the Supplementary Information. When measured as a film or at open circuit potential (OCP), **RhGNR-2DNS** exhibited an edge energy characteristic of Rh(III) (23.224 keV) according to reference samples (Figure 6a and b). Notably, **RhGNR-2DNS** had a slightly higher edge energy (0.3 eV) than **Rh-bpds** which was attributed to the more electron-withdrawing character of the GNR ligand (Figure S16a). Under applied potentials more negative than the onset of HER (-0.5 and -1.3 V vs. NHE at pH 2 and 13, respectively) an evident ~2 eV shift to lower edge energies was detected which was indicative of a 2-electron Rh-centered reduction to its +1 oxidation state (Figure 6 a and b), indicating that the bottleneck intermediate in the catalytic cycle is some form of a two-electron reduced Rh(I) intermediate of **RhGNR-2DNS.** This striking observation diverges from models put forward for strongly coupled molecular catalysts grafted onto conductive electrodes,[35,36] and further supports our conclusion that the electrocatalytic behavior of **RhGNR-2DNS** is not affected by the interfacial electric fields. The observation of Rh(I) species as the longest-lived intermediate aligns with previous mechanistic studies of molecular catalysts by Blakemore and co-authors, where the longest-lived intermediate is proposed to involve the Rh(I) species with protonated Cp* ligands.[22] Based on these results, we hypothesize that the HER by

RhGNR-2DNS follows a mechanism that is similar to that observed for molecular species and involves the protonation of two-electron reduced Rh(I) species and subsequent tautomerization to form Rh(I)Cp*–H, as illustrated in Scheme 3.

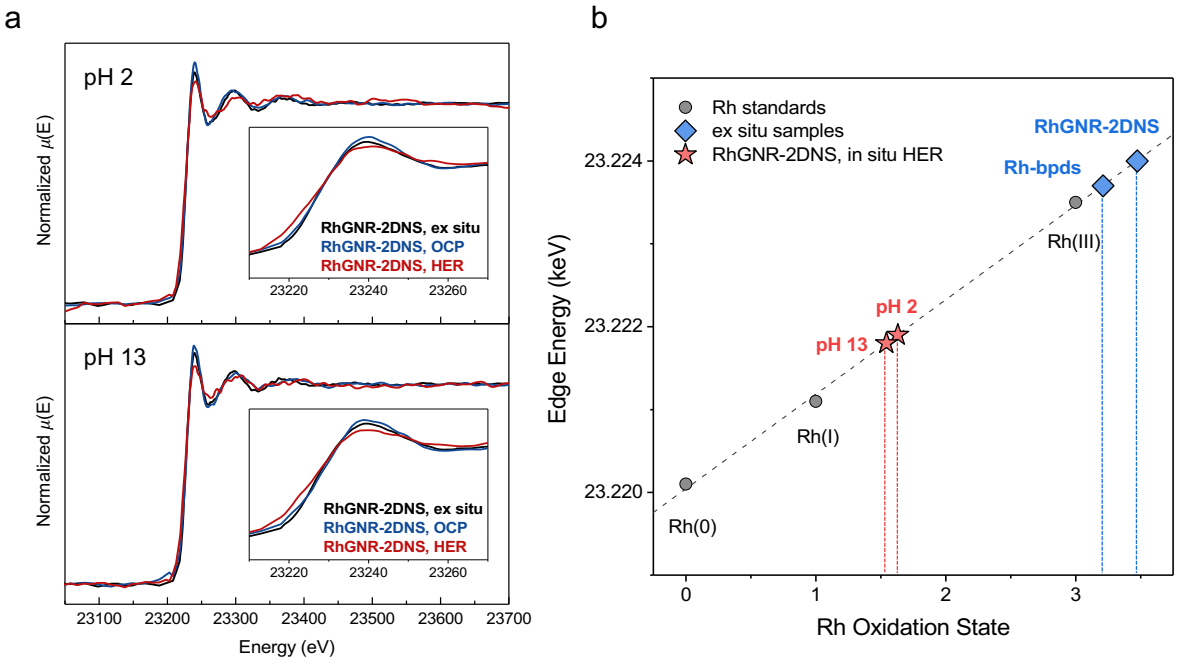

Figure 6. a) Grazing incidence X-ray absorption near edge structure (XANES) data of **RhGNR-2DNS** recorded at pH 2 and 13. The samples were measured as ex situ (black spectra), at open circuit potential (OCP, blue spectra) and at constant applied potentials more negative than the onset for HER (red spectra) which were -0.5 V and -1.3 V vs. NHE for pH 2 and 13, respectively. The inset shows a clear edge shift to lower energies under HER conditions indicating a net reduction in the Rh oxidation state. b) Determination of Rh oxidation state in **RhGNR-2DNS** and **Rh-bpds** samples based on calibration with a Rh(0), Rh(I) and Rh(III) reference.

The question remains why does **RhGNR-2DNS** maintain catalytic activity throughout the entire pH region, while the model compounds **Rh-bpds** and **Rh-bpm** appear to lose the catalytic behavior at pH values above 8.1 and 10.1, respectively. Taking together data from in situ Rh K-edge GI-XANES and our insights from Pourbaix slope analysis, we concluded that strong

electronic coupling and local electric field effects are not likely factors which explain the retained HER activity in **RhGNR-2DNS**. The Rh K-edge shift observed during in situ GI-XANES suggests that Rh sites on **RhGNR-2DNS** were not strongly coupled to glassy carbon electrodes. In previous studies on grafted molecular systems, the lack of metal K-edge shifts were used as evidence for strong electronic coupling and true hybridization between catalyst and electrode. Our analysis of the Pourbaix slopes indicated that **RhGNR-2DNS** experience only 15% of the interfacial potential (***f*** value of 0.15). This small value of ***f*** is quite reasonable considering that Rh atoms on **RhGNR-2DNS** were expected to be positioned at the far edge of the electrical double layer (EDL) (~1.7 nm from the electrode), where local electric fields have largely decayed. Such a small value of ***f*** may be capable of providing the added "push" needed to drive protonation at reduced Rh sites, however it cannot be confidently stated to account for the changed reactivity and thus a molecular picture of the operative HER mechanism is most appropriate (Scheme 3).

Our investigations suggest that broadened HER activity of **RhGNR-2DNS**, as compared to our molecular model compounds, can be ascribed to the "responsive" nature of the bipyrimidine-based ligands, which host PCET. HER activity of the **Rh-bpds** model was lost beyond pH 8, a result associated with diminished driving force for protonation of the Rh(I) intermediate. Computational analysis reinforced this by predicting an 8 or 14 pK_a unit increase to the Rh(I) basicity for the dihydro (H_2) or hydrido (H^-) versions of hydrogenated bipyrimidine-based ligands, respectively (Table S6). The increased basicity was seemingly uninfluenced by the bipyrimidine-based ligand size, which was confirmed by surveying additional model compounds with the phenanthroline- and benzoperylene-based ligands as shown in Figure S14. For **Rh-bpm**, while we did observe an extension of the operative pH window (up to pH 10.1), the activity was curtailed by film formation which passivated the electrode. Conversely, the ordered **RhGNR-2DNS** films exhibit sustained HER activity across the entire aqueous pH window which was attributable to the elevated basicity of Rh(I) intermediates bestowed by the responsive PCET-hosting GNR ligand. Such findings demonstrate the pivotal role of ligand design in predicting and optimizing the behavior of metal-centered electrocatalysts for efficient energy conversion.

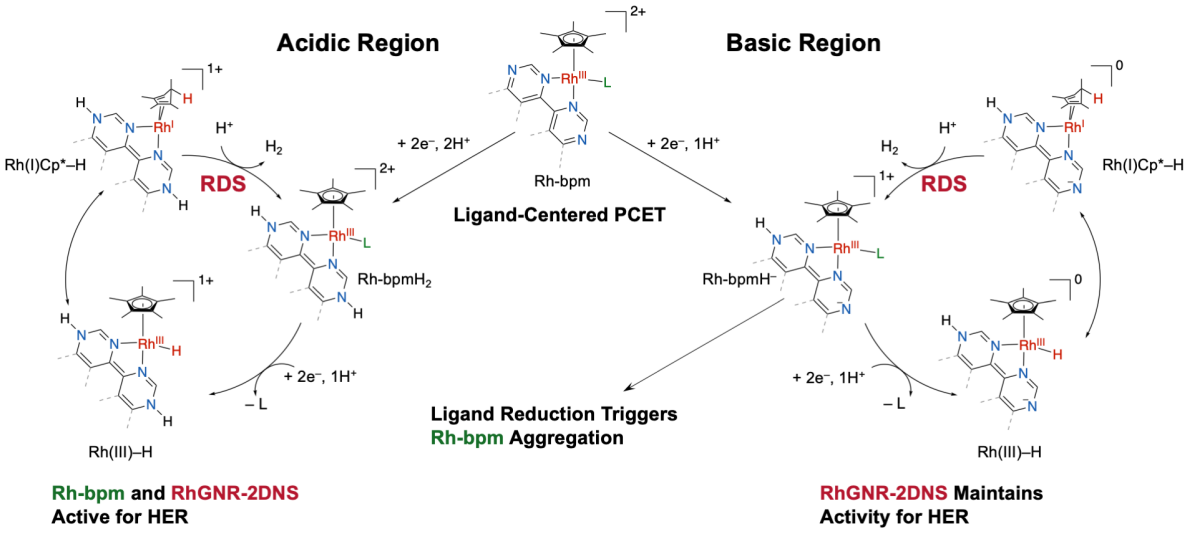

Scheme 3. Proposed HER pathway for **Rh-bpm** and **RhGNR-2DNS** in acidic (Left) and basic (Right) conditions. In both cases, HER is preceded by PCET at the bipyrimidine moiety which generates the active form of the catalyst. The rate-determining step (RDS) is proposed to involve the Rh(I)Cp*–H intermediate involved in molecular HER pathways.[22] **Rh-bpm** lost activity in basic pHs resulting from ligand-centered reduction-induced aggregation.

Conclusions

In conclusion, we report an electrochemical investigation of self-assembled GNR films (**GNR-2DNS**) and Rh-coordinated GNR films (**RhGNR-2DNS**) on electrode surfaces. We developed an indirect method to probe the interfacial potential experienced by the nanosheets at the electrode/electrolyte interface. Our method involves experimentally obtaining the Pourbaix slopes associated with PCET on nanoribbon bipyrimidine units and fitting the resulting slopes to a theoretical model that allows the derivation of the parameter ***f***, which represents the fraction of the interfacial potential drop experienced by the redox-active group. Our analysis revealed an interesting outcome: **GNR-2DNS** experiences fully the inner potential of the working electrode (***f*** = 1), indicating the lack of charge screening by the electrolyte ions in the plane of the redox-active PCET groups of **GNR-2DNS**. This "strongly coupled" behavior shows that non-covalent interactions can be utilized to immobilize molecular functional groups onto electrode surfaces for field-driven chemistry. However, the fraction of interfacial potential experienced by **RhGNR-2DNS** was found to be much smaller (***f*** value of only 0.15), suggesting that Rh-coordinated

bipyrimidine sites of **RhGNR-2DNS** are positioned near the edge of the EDL wherein interfacial potentials have largely decayed.

Our investigation of HER activity has shown that **RhGNR-2DNS** exhibit significantly improved catalytic performance relative to two molecular model compounds, **Rh-bpds** and **Rh-bpm**. In specific, the molecular models were shown to lose their activity in the basic pH region, while **RhGNR-2DNS** remains HER-active throughout the entire aqueous pH domain (pH 0 – 14) with catalytic onset changing by a slope of –59 mV per pH unit. The dramatically improved HER performance was assigned to two factors which underscore the importance of ligand design and macroscopic assembly for developing active and robust electrocatalysts: 1) the "responsive" nature of bipyrimidine-based ligands, which play host to their own PCET-process, dramatically altered the driving force for crucial protonation steps at reduced Rh intermediates. 2) Our immobilization approach, which forms highly ordered films of **RhGNR-2DNS**, prevented the aggregation which was responsible for attenuating the HER activity of **Rh-bpm**.

Acknowledgements

This research was supported by the National Science Foundation through NSF grant #2102247. We thank the Laboratory Computing Resources Center (LCRC) at Argonne National Laboratory (ANL) for the advanced computing resources used for DFT calculations. We also thank the Advanced Photon Source (APS), specifically beamlines 10-BM and 20-BM, at ANL where all Rh K-edge X-ray absorption measurements were conducted. We also thank the Electron Microscopy Core and the Nanotechnology Core Facility, which are both a part of UIC's Research Resources Center (RRC) and is where all XPS, SEM and AFM characterization was performed.

References

(1) Ehlers, J. C.; Feidenhans'l, A. A.; Therkildsen, K. T.; Larrazábal, G. O. Affordable Green Hydrogen from Alkaline Water Electrolysis: Key Research Needs from an Industrial Perspective. *ACS Energy Lett.* **2023**, *8* (3), 1502–1509. https://doi.org/10.1021/acsenergylett.2c02897.

(2) Helm, M. L.; Stewart, M. P.; Bullock, R. M.; DuBois, M. R.; DuBois, D. L. A Synthetic Nickel Electrocatalyst with a Turnover Frequency Above 100,000 S−1 for H2 Production.

Science (80-.). **2011**, *333* (6044), 863–866. https://doi.org/10.1126/science.1205864.

(3) Dempsey, J. L.; Brunschwig, B. S.; Winkler, J. R.; Gray, H. B. Hydrogen Evolution Catalyzed by Cobaloximes. *Acc. Chem. Res.* **2009**, *42* (12), 1995–2004. https://doi.org/10.1021/ar900253e.

(4) Bhugun, I.; Lexa, D.; Savéant, J.-M. Homogeneous Catalysis of Electrochemical Hydrogen Evolution by Iron(0) Porphyrins. *J. Am. Chem. Soc.* **1996**, *118* (16), 3982–3983. https://doi.org/10.1021/ja954326x.

(5) Kaur-Ghumaan, S.; Schwartz, L.; Lomoth, R.; Stein, M.; Ott, S. Catalytic Hydrogen Evolution from Mononuclear Iron(II) Carbonyl Complexes as Minimal Functional Models of the [FeFe] Hydrogenase Active Site. *Angew. Chemie Int. Ed.* **2010**, *49* (43), 8033–8036. https://doi.org/https://doi.org/10.1002/anie.201002719.

(6) Kaeffer, N.; Chavarot-Kerlidou, M.; Artero, V. Hydrogen Evolution Catalyzed by Cobalt Diimine–Dioxime Complexes. *Acc. Chem. Res.* **2015**, *48* (5), 1286–1295. https://doi.org/10.1021/acs.accounts.5b00058.

(7) Wilson, A. D.; Newell, R. H.; McNevin, M. J.; Muckerman, J. T.; Rakowski DuBois, M.; DuBois, D. L. Hydrogen Oxidation and Production Using Nickel-Based Molecular Catalysts with Positioned Proton Relays. *J. Am. Chem. Soc.* **2006**, *128* (1), 358–366. https://doi.org/10.1021/ja056442y.

(8) Brazzolotto, D.; Gennari, M.; Queyriaux, N.; Simmons, T. R.; Pécaut, J.; Demeshko, S.; Meyer, F.; Orio, M.; Artero, V.; Duboc, C. Nickel-Centred Proton Reduction Catalysis in a Model of [NiFe] Hydrogenase. *Nat. Chem.* **2016**, *8* (11), 1054–1060. https://doi.org/10.1038/nchem.2575.

(9) Brecht, M.; van Gastel, M.; Buhrke, T.; Friedrich, B.; Lubitz, W. Direct Detection of a Hydrogen Ligand in the [NiFe] Center of the Regulatory H2-Sensing Hydrogenase from Ralstonia Eutropha in Its Reduced State by HYSCORE and ENDOR Spectroscopy. *J. Am. Chem. Soc.* **2003**, *125* (43), 13075–13083. https://doi.org/10.1021/ja036624x.

(10) Karunadasa, H. I.; Chang, C. J.; Long, J. R. A Molecular Molybdenum-Oxo Catalyst for Generating Hydrogen from Water. *Nature* **2010**, *464* (7293), 1329–1333. https://doi.org/10.1038/nature08969.

(11) Karunadasa, H. I.; Montalvo, E.; Sun, Y.; Majda, M.; Long, J. R.; Chang, C. J. A Molecular MoS2 Edge Site Mimic for Catalytic Hydrogen Generation. *Science (80-.)*.

2012, *335* (6069), 698–702. https://doi.org/10.1126/science.1215868.

(12) McNamara, W. R.; Han, Z.; Alperin, P. J.; Brennessel, W. W.; Holland, P. L.; Eisenberg, R. A Cobalt–Dithiolene Complex for the Photocatalytic and Electrocatalytic Reduction of Protons. *J. Am. Chem. Soc.* **2011**, *133* (39), 15368–15371. https://doi.org/10.1021/ja207842r.

(13) Stubbert, B. D.; Peters, J. C.; Gray, H. B. Rapid Water Reduction to H2 Catalyzed by a Cobalt Bis(Iminopyridine) Complex. *J. Am. Chem. Soc.* **2011**, *133* (45), 18070–18073. https://doi.org/10.1021/ja2078015.

(14) Kölle, U.; Grützel, M. Organometallic Rhodium(III) Complexes as Catalysts for the Photoreduction of Protons to Hydrogen on Colloidal TiO2. *Angew. Chemie Int. Ed. English* **1987**, *26* (6), 567–570. https://doi.org/https://doi.org/10.1002/anie.198705671.

(15) Cosnier, S.; Deronzier, A.; Vlachopoulos, N. Carbon/Poly {pyrrole-[(C5Me5)Rh(Bpy)Cl]+} Modified Electrodes; a Molecularly-Based Material for Hydrogen Evolution (Bpy = 2{,}2′-Bipyridine). *J. Chem. Soc.{,} Chem. Commun.* **1989**, No. 17, 1259–1261. https://doi.org/10.1039/C39890001259.

(16) Blakemore, J. D.; Hernandez, E. S.; Sattler, W.; Hunter, B. M.; Henling, L. M.; Brunschwig, B. S.; Gray, H. B. Pentamethylcyclopentadienyl Rhodium Complexes. *Polyhedron* **2014**, *84*, 14–18. https://doi.org/https://doi.org/10.1016/j.poly.2014.05.022.

(17) Lionetti, D.; Day, V. W.; Blakemore, J. D. Synthesis and Electrochemical Properties of Half-Sandwich Rhodium and Iridium Methyl Complexes. *Organometallics* **2017**, *36* (10), 1897–1905. https://doi.org/10.1021/acs.organomet.7b00136.

(18) Pitman, C. L.; Finster, O. N. L.; Miller, A. J. M. Cyclopentadiene-Mediated Hydride Transfer from Rhodium Complexes. *Chem. Commun.* **2016**, *52* (58), 9105–9108. https://doi.org/10.1039/C6CC00575F.

(19) Quintana, L. M. A.; Johnson, S. I.; Corona, S. L.; Villatoro, W.; Goddard, W. A.; Takase, M. K.; VanderVelde, D. G.; Winkler, J. R.; Gray, H. B.; Blakemore, J. D. Proton{\textendash}hydride Tautomerism in Hydrogen Evolution Catalysis. *Proc. Natl. Acad. Sci.* **2016**, *113* (23), 6409–6414. https://doi.org/10.1073/pnas.1606018113.

(20) Peng, Y.; Ramos-Garcés, M. V; Lionetti, D.; Blakemore, J. D. Structural and Electrochemical Consequences of [Cp*] Ligand Protonation. *Inorg. Chem.* **2017**, *56* (17), 10824–10831. https://doi.org/10.1021/acs.inorgchem.7b01895.

(21) Johnson, S. I.; Gray, H. B.; Blakemore, J. D.; Goddard, W. A. I. I. I. Role of Ligand Protonation in Dihydrogen Evolution from a Pentamethylcyclopentadienyl Rhodium Catalyst. *Inorg. Chem.* **2017**, *56* (18), 11375–11386. https://doi.org/10.1021/acs.inorgchem.7b01698.

(22) Henke, W. C.; Peng, Y.; Meier, A. A.; Fujita, E.; Grills, D. C.; Polyansky, D. E.; Blakemore, J. D. Mechanistic Roles of Metal- and Ligand-Protonated Species in Hydrogen Evolution with [Cp*Rh] Complexes. *Proc. Natl. Acad. Sci.* **2023**, *120* (21), e2217189120. https://doi.org/10.1073/pnas.2217189120.

(23) Ruppert, R.; Herrmann, S.; Steckhan, E. Very Efficient Reduction of NAD(P)+ with Formate Catalysed by Cationic Rhodium Complexes. *J. Chem. Soc. Chem. Commun.* **1988**, No. 17, 1150–1151. https://doi.org/10.1039/C39880001150.

(24) Steckhan, E.; Herrmann, S.; Ruppert, R.; Dietz, E.; Frede, M.; Spika, E. Analytical Study of a Series of Substituted (2,2'-Bipyridyl)(Pentamethylcyclopentadienyl)Rhodium and -Iridium Complexes with Regard to Their Effectiveness as Redox Catalysts for the Indirect Electrochemical and Chemical Reduction of NAD(P)+. *Organometallics* **1991**, *10* (5), 1568–1577. https://doi.org/10.1021/om00051a056.

(25) Lo, H. C.; Leiva, C.; Buriez, O.; Kerr, J. B.; Olmstead, M. M.; Fish, R. H. Bioorganometallic Chemistry. 13. Regioselective Reduction of NAD+ Models, 1-Benzylnicotinamde Triflate and β-Nicotinamide Ribose-5'-Methyl Phosphate, with in Situ Generated [Cp*Rh(Bpy)H]+: Structure−Activity Relationships, Kinetics, and Mechanistic Aspec. *Inorg. Chem.* **2001**, *40* (26), 6705–6716. https://doi.org/10.1021/ic010562z.

(26) Thorogood, C. A.; Wildgoose, G. G.; Crossley, A.; Jacobs, R. M. J.; Jones, J. H.; Compton, R. G. Differentiating between Ortho- and Para-Quinone Surface Groups on Graphite, Glassy Carbon, and Carbon Nanotubes Using Organic and Inorganic Voltammetric and X-Ray Photoelectron Spectroscopy Labels. *Chem. Mater.* **2007**, *19* (20), 4964–4974. https://doi.org/10.1021/cm071412a.

(27) Delamar, M.; Hitmi, R.; Pinson, J.; Saveant, J. M. Covalent Modification of Carbon Surfaces by Grafting of Functionalized Aryl Radicals Produced from Electrochemical Reduction of Diazonium Salts. *J. Am. Chem. Soc.* **1992**, *114* (14), 5883–5884. https://doi.org/10.1021/ja00040a074.

(28) Oh, S.; Gallagher, J. R.; Miller, J. T.; Surendranath, Y. Graphite-Conjugated Rhenium

Catalysts for Carbon Dioxide Reduction. *J. Am. Chem. Soc.* **2016**, *138* (6), 1820–1823.

(29) Heo, J.; Ahn, H.; Won, J.; Son, J. G.; Shon, H. K.; Lee, T. G.; Han, S. W.; Baik, M.-H. Electro-Inductive Effect: Electrodes as Functional Groups with Tunable Electronic Properties. *Science (80-.).* **2020**, *370* (6513), 214–219. https://doi.org/10.1126/science.abb6375.

(30) Bhattacharyya, D.; Videla, P. E.; Cattaneo, M.; Batista, V. S.; Lian, T.; Kubiak, C. P. Vibrational Stark Shift Spectroscopy of Catalysts under the Influence of Electric Fields at Electrode–Solution Interfaces. *Chem. Sci.* **2021**, *12* (30), 10131–10149. https://doi.org/10.1039/D1SC01876K.

(31) Delley, M. F.; Nichols, E. M.; Mayer, J. M. Interfacial Acid–Base Equilibria and Electric Fields Concurrently Probed by In Situ Surface-Enhanced Infrared Spectroscopy. *J. Am. Chem. Soc.* **2021**, *143* (28), 10778–10792. https://doi.org/10.1021/jacs.1c05419.

(32) Bhattacharyya, D.; Videla, P. E.; Palasz, J. M.; Tangen, I.; Meng, J.; Kubiak, C. P.; Batista, V. S.; Lian, T. Sub-Nanometer Mapping of the Interfacial Electric Field Profile Using a Vibrational Stark Shift Ruler. *J. Am. Chem. Soc.* **2022**, *144* (31), 14330–14338. https://doi.org/10.1021/jacs.2c05563.

(33) Jackson, M. N.; Oh, S.; Kaminsky, C. J.; Chu, S. B.; Zhang, G.; Miller, J. T.; Surendranath, Y. Strong Electronic Coupling of Molecular Sites to Graphitic Electrodes via Pyrazine Conjugation. *J. Am. Chem. Soc.* **2018**, *140* (3), 1004–1010. https://doi.org/10.1021/jacs.7b10723.

(34) Kaminsky, C. J.; Wright, J.; Surendranath, Y. Graphite-Conjugation Enhances Porphyrin Electrocatalysis. *ACS Catal.* **2019**, *9* (4), 3667–3671. https://doi.org/10.1021/acscatal.9b00404.

(35) Jackson, M. N.; Kaminsky, C. J.; Oh, S.; Melville, J. F.; Surendranath, Y. Graphite Conjugation Eliminates Redox Intermediates in Molecular Electrocatalysis. *J. Am. Chem. Soc.* **2019**, *141* (36), 14160–14167.

(36) Jackson, M. N.; Surendranath, Y. Molecular Control of Heterogeneous Electrocatalysis through Graphite Conjugation. *Acc. Chem. Res.* **2019**, *52* (12), 3432–3441.

(37) Jackson, M. N.; Pegis, M. L.; Surendranath, Y. Graphite-Conjugated Acids Reveal a Molecular Framework for Proton-Coupled Electron Transfer at Electrode Surfaces. *ACS Cent. Sci.* **2019**, *5* (5), 831–841. https://doi.org/10.1021/acscentsci.9b00114.

(38) Warburton, R. E.; Hutchison, P.; Jackson, M. N.; Pegis, M. L.; Surendranath, Y.; Hammes-Schiffer, S. Interfacial Field-Driven Proton-Coupled Electron Transfer at Graphite-Conjugated Organic Acids. *J. Am. Chem. Soc.* **2020**, *142* (49), 20855–20864. https://doi.org/10.1021/jacs.0c10632.

(39) Hutchison, P.; Warburton, R. E.; Surendranath, Y.; Hammes-Schiffer, S. Correlation between Electronic Descriptor and Proton-Coupled Electron Transfer Thermodynamics in Doped Graphite-Conjugated Catalysts. *J. Phys. Chem. Lett.* **2022**, *13* (48), 11216–11222. https://doi.org/10.1021/acs.jpclett.2c03278.

(40) Ghosh, M.; Braley, S. E.; Ezhov, R.; Worster, H.; Valdez-Moreira, J. A.; Losovyj, Y.; Jakubikova, E.; Pushkar, Y. N.; Smith, J. M. A Spectroscopically Observed Iron Nitrosyl Intermediate in the Reduction of Nitrate by a Surface-Conjugated Electrocatalyst. *J. Am. Chem. Soc.* **2022**, *144* (39), 17824–17831. https://doi.org/10.1021/jacs.2c03487.

(41) Barman, K.; Askarova, G.; Jia, R.; Hu, G.; Mirkin, M. V. Efficient Voltage-Driven Oxidation of Water and Alcohols by an Organic Molecular Catalyst Directly Attached to a Carbon Electrode. *J. Am. Chem. Soc.* **2023**, *145* (10), 5786–5794. https://doi.org/10.1021/jacs.2c12775.

(42) Barman, K.; Chen, Y.; Wu, S.; Hu, G.; Mirkin, M. V. Voltage-Driven Molecular Catalysis: A Promising Approach to Electrosynthesis. *ACS Catal.* **2023**, *13* (24), 15869–15876. https://doi.org/10.1021/acscatal.3c03644.

(43) Barman, K.; Wang, X.; Jia, R.; Mirkin, M. V. Mediated Charge Transfer at Nanoelectrodes: A New Approach to Electrochemical Reactivity Mapping and Nanosensing. *J. Am. Chem. Soc.* **2021**, *143* (23), 8547–8551. https://doi.org/10.1021/jacs.1c02532.

(44) Barman, K.; Wang, X.; Jia, R.; Askarova, G.; Hu, G.; Mirkin, M. V. Voltage-Driven Molecular Catalysis of Electrochemical Reactions. *J. Am. Chem. Soc.* **2021**, *143* (42), 17344–17347. https://doi.org/10.1021/jacs.1c07934.

(45) Gorin, C. F.; Beh, E. S.; Bui, Q. M.; Dick, G. R.; Kanan, M. W. Interfacial Electric Field Effects on a Carbene Reaction Catalyzed by Rh Porphyrins. *J. Am. Chem. Soc.* **2013**, *135* (30), 11257–11265. https://doi.org/10.1021/ja404394z.

(46) Kaminsky, C. J.; Weng, S.; Wright, J.; Surendranath, Y. Adsorbed Cobalt Porphyrins Act like Metal Surfaces in Electrocatalysis. *Nat. Catal.* **2022**, *5* (5), 430–442.

https://doi.org/10.1038/s41929-022-00791-6.

(47) Zhanaidarova, A.; Jones, S. C.; Despagnet-Ayoub, E.; Pimentel, B. R.; Kubiak, C. P. Re(TBu-Bpy)(CO)3Cl Supported on Multi-Walled Carbon Nanotubes Selectively Reduces CO2 in Water. *J. Am. Chem. Soc.* **2019**, *141* (43), 17270–17277. https://doi.org/10.1021/jacs.9b08445.

(48) Costentin, C.; Dridi, H.; Savéant, J.-M. Molecular Catalysis of O2 Reduction by Iron Porphyrins in Water: Heterogeneous versus Homogeneous Pathways. *J. Am. Chem. Soc.* **2015**, *137* (42), 13535–13544. https://doi.org/10.1021/jacs.5b06834.

(49) Hutchison, P.; Kaminsky, C. J.; Surendranath, Y.; Hammes-Schiffer, S. Concerted Proton-Coupled Electron Transfer to a Graphite Adsorbed Metalloporphyrin Occurs by Band to Bond Electron Redistribution. *ACS Cent. Sci.* **2023**, *9* (5), 927–936. https://doi.org/10.1021/acscentsci.3c00186.

(50) Wu, Y.; Jiang, Z.; Lu, X.; Liang, Y.; Wang, H. Domino Electroreduction of CO 2 to Methanol on a Molecular Catalyst. *Nature* **2019**, *575* (7784), 639–642.

(51) Wang, M.; Torbensen, K.; Salvatore, D.; Ren, S.; Joulié, D.; Dumoulin, F.; Mendoza, D.; Lassalle-Kaiser, B.; Işci, U.; Berlinguette, C. P.; et al. CO2 Electrochemical Catalytic Reduction with a Highly Active Cobalt Phthalocyanine. *Nat. Commun.* **2019**, *10* (1), 3602. https://doi.org/10.1038/s41467-019-11542-w.

(52) Boutin, E.; Wang, M.; Lin, J. C.; Mesnage, M.; Mendoza, D.; Lassalle-Kaiser, B.; Hahn, C.; Jaramillo, T. F.; Robert, M. Aqueous Electrochemical Reduction of Carbon Dioxide and Carbon Monoxide into Methanol with Cobalt Phthalocyanine. *Angew. Chemie Int. Ed.* **2019**, *58* (45), 16172–16176.

(53) Ren, S.; Joulié, D.; Salvatore, D.; Torbensen, K.; Wang, M.; Robert, M.; Berlinguette, C. P. Molecular Electrocatalysts Can Mediate Fast, Selective CO2 Reduction in a Flow Cell. *Science (80-.).* **2019**, *365* (6451), 367–369. https://doi.org/10.1126/science.aax4608.

(54) Wu, Y.; Hu, G.; Rooney, C. L.; Brudvig, G. W.; Wang, H. Heterogeneous Nature of Electrocatalytic CO/CO2 Reduction by Cobalt Phthalocyanines. *ChemSusChem* **2020**, *13* (23), 6296–6299.

(55) Su, J.; Musgrave, C. B.; Song, Y.; Huang, L.; Liu, Y.; Li, G.; Xin, Y.; Xiong, P.; Li, M. M.-J.; Wu, H.; et al. Strain Enhances the Activity of Molecular Electrocatalysts via Carbon Nanotube Supports. *Nat. Catal.* **2023**, *6* (9), 818–828.

https://doi.org/10.1038/s41929-023-01005-3.

(56) Vo, T. H.; Perera, U. G. E.; Shekhirev, M.; Mehdi Pour, M.; Kunkel, D. A.; Lu, H.; Gruverman, A.; Sutter, E.; Cotlet, M.; Nykypanchuk, D.; et al. Nitrogen-Doping Induced Self-Assembly of Graphene Nanoribbon-Based Two-Dimensional and Three-Dimensional Metamaterials. *Nano Lett.* **2015**, *15* (9), 5770–5777. https://doi.org/10.1021/acs.nanolett.5b01723.

(57) Zoric, M. R.; Askins, E. J.; Qiao, X.; Glusac, K. D. Strong Electronic Coupling of Graphene Nanoribbons onto Basal Plane of a Glassy Carbon Electrode. *ACS Appl. Electron. Mater.* **2021**, *3* (2), 854–860. https://doi.org/10.1021/acsaelm.0c00978.

(58) Morgenroth, F.; Reuther, E.; Müllen, K. Polyphenylene Dendrimers: From Three-Dimensional to Two-Dimensional Structures. *Angew. Chemie Int. Ed. English* **1997**, *36* (6), 631–634. https://doi.org/https://doi.org/10.1002/anie.199706311.

(59) Langmuir, I.; Schaefer, V. J. Activities of Urease and Pepsin Monolayers. *J. Am. Chem. Soc.* **1938**, *60* (6), 1351–1360. https://doi.org/10.1021/ja01273a023.

(60) Shekhirev, M.; Vo, T. H.; Mehdi Pour, M.; Lipatov, A.; Munukutla, S.; Lyding, J. W.; Sinitskii, A. Interfacial Self-Assembly of Atomically Precise Graphene Nanoribbons into Uniform Thin Films for Electronics Applications. *ACS Appl. Mater. Interfaces* **2017**, *9* (1), 693–700. https://doi.org/10.1021/acsami.6b12508.

(61) Lazar, P.; Mach, R.; Otyepka, M. Spectroscopic Fingerprints of Graphitic, Pyrrolic, Pyridinic, and Chemisorbed Nitrogen in N-Doped Graphene. *J. Phys. Chem. C* **2019**, *123* (16), 10695–10702.

(62) Ramaswamy, N.; Tylus, U.; Jia, Q.; Mukerjee, S. Activity Descriptor Identification for Oxygen Reduction on Nonprecious Electrocatalysts: Linking Surface Science to Coordination Chemistry. *J. Am. Chem. Soc.* **2013**, *135* (41), 15443–15449.

(63) Brunetti, B.; De Giglio, E.; Cafagna, D.; Desimoni, E. XPS Analysis of Glassy Carbon Electrodes Chemically Modified with 8-Hydroxyquinoline-5-Sulphonic Acid. *Surf. Interface Anal.* **2012**, *44* (4), 491–496. https://doi.org/https://doi.org/10.1002/sia.3880.

(64) Naumkin, A.; Kraut-Vass, A.; Gaarenstroom, S. W.; Powell, C. J. NIST X-Ray Photoelectron Spectroscopy Database. *NIST Stand. Ref. Database 20* **2000**.

(65) Soldevila-Barreda, J. J.; Habtemariam, A.; Romero-Canelón, I.; Sadler, P. J. Half-Sandwich Rhodium(III) Transfer Hydrogenation Catalysts: Reduction of NAD+ and

Pyruvate, and Antiproliferative Activity. *J. Inorg. Biochem.* **2015**, *153*, 322–333. https://doi.org/https://doi.org/10.1016/j.jinorgbio.2015.10.008.

(66) Ravel, B.; Newville, M. ATHENA, ARTEMIS, HEPHAESTUS: Data Analysis for X-Ray Absorption Spectroscopy Using IFEFFIT. *J. Synchrotron Radiat.* **2005**, *12* (4), 537–541. https://doi.org/https://doi.org/10.1107/S0909049505012719.

(67) Sieger, M.; Kaim, W.; Stufkens, D. J.; Snoeck, T. L.; Stoll, H.; Záliš, S. Reduced and Excited States of the Intermediates (α-Diimine)(C5R5)Rh in Hydride Transfer Catalysis Schemes: EPR and Resonance Raman Spectroscopy, and Comparative DFT Calculations of Co, Rh and Ir Analogues. *Dalt. Trans.* **2004**, No. 22, 3815–3821. https://doi.org/10.1039/B411892H.

(68) Drummer, M. C.; Weerasooriya, R. B.; Gupta, N.; Phelan, B. T.; Valentine, A. J. S.; Cordones, A. A.; Li, X.; Chen, L. X.; Glusac, K. D. Long-Lived Excited State in a Solubilized Graphene Nanoribbon. *J. Phys. Chem. C* **2022**, *126* (4), 1946–1957. https://doi.org/10.1021/acs.jpcc.1c10024.

(69) Owhoso, F. V; Modak, S. V; Saha, P.; Kwabi, D. G. Effect of Covalent Modification on Proton-Coupled Electron Transfer at Quinone-Functionalized Carbon Electrodes. *J. Phys. Chem. C* **2023**, *127* (6), 3165–3175. https://doi.org/10.1021/acs.jpcc.2c06356.

(70) Smith, C. P.; White, H. S. Theory of the Interfacial Potential Distribution and Reversible Voltammetric Response of Electrodes Coated with Electroactive Molecular Films. *Anal. Chem.* **1992**, *64* (20), 2398–2405. https://doi.org/10.1021/ac00044a017.

(71) Weinberg, D. R.; Gagliardi, C. J.; Hull, J. F.; Murphy, C. F.; Kent, C. A.; Westlake, B. C.; Paul, A.; Ess, D. H.; McCafferty, D. G.; Meyer, T. J. Proton-Coupled Electron Transfer. *Chem. Rev.* **2012**, *112* (7), 4016–4093. https://doi.org/10.1021/cr200177j.